



## Article

# Spatiotemporally Mapping Non-Grain Production of Winter Wheat Using a Developed Auto-Generating Sample Algorithm on Google Earth Engine

Meng Zhang <sup>1,2</sup> , Peijun Sun <sup>1,2,\*</sup> and Zhangli Sun <sup>3</sup>

<sup>1</sup> Shaanxi Key Laboratory of Earth Surface System and Environmental Carrying Capacity, Northwest University, Xi'an 710127, China; zhangmeng3@stumail.nwu.edu.cn

<sup>2</sup> College of Urban and Environmental Sciences, Northwest University, Xi'an 710127, China

<sup>3</sup> College of Earth Sciences, Chengdu University of Technology, Chengdu 610059, China; sunzhangli@cdut.edu.cn

\* Correspondence: sunpeijun02@nwu.edu.cn

**Abstract:** Spatiotemporally mapping winter wheat is imperative for informing and shaping global food security policies. Traditional mapping methods heavily rely on sufficient and reliable samples obtained through labor-intensive fieldwork and manual sample collection. However, these methods are time-consuming, costly, and lack timely and continuous data collection. To address these challenges and fully leverage remote sensing big data and cloud computing platforms like Google Earth Engine (GEE), this paper developed an algorithm for Auto-Generating Winter Wheat Samples for mapping (AGWWS). The AGWWS utilizes historical samples to determine the optimal migration threshold by measuring Spectral Angle Distance (SAD), Euclidean Distance (ED), and Near-Infrared band Difference Index (NIRDI). This facilitates the auto-generation of winter wheat sample sets for the years 2000, 2005, 2010, 2015, and 2021. Approximately two-thirds of the samples were allocated for training, with the remaining one-third used for validating the mapping method, employing the One-Class Support Vector Machine (OCSVM). The Huang–Huai–Hai (HHH) Plain, a major winter wheat production region, was selected to perform the algorithm and subsequent analysis on. Different combinations of the hyper-parameters, gamma and nu, of the OCSVM based on the Gaussian Radial Basis Function Kernel were tested for each year. Following correlation analysis between the winter wheat area derived from the generated maps and the national statistical dataset at the city level, the map with the highest corresponding  $R^2$  was chosen as the AGWWS map for each year (0.77, 0.77, 0.80, 0.86, and 0.87 for 2000, 2005, 2010, 2015, and 2021, respectively). The AGWWS maps ultimately achieved an average Overall Accuracy of 81.65%. The study then explores the Non-Grain Production of Winter Wheat (NGPOWW) by analyzing winter wheat change maps from 2000–2005, 2005–2010, 2005–2010, and 2015–2021 in the HHH Plain. Despite an overall increase in the total planted area of winter wheat, the NGPOWW phenomena has led to concerning winter wheat planting marginalization. Compensatory winter wheat areas are notably situated in mountainous and suburban cultivated lands with low qualities. Consequently, despite the apparent expansion in planted areas, winter wheat production is anticipated to be adversely affected. The findings highlight the necessity for improved cultivated land protection policies monitoring the land quality of the compensation and setting strict quota limits on occupations.



**Citation:** Zhang, M.; Sun, P.; Sun, Z. Spatiotemporally Mapping Non-Grain Production of Winter Wheat Using a Developed Auto-Generating Sample Algorithm on Google Earth Engine. *Remote Sens.* **2024**, *16*, 659. <https://doi.org/10.3390/rs16040659>

Academic Editors: Jochem Verrelst, Clement Atzberger, Egor Prikaziuk and Katja Berger

Received: 28 December 2023

Revised: 3 February 2024

Accepted: 8 February 2024

Published: 11 February 2024



**Copyright:** © 2024 by the authors. Licensee MDPI, Basel, Switzerland. This article is an open access article distributed under the terms and conditions of the Creative Commons Attribution (CC BY) license (<https://creativecommons.org/licenses/by/4.0/>).

**Keywords:** winter wheat; auto-generating sample algorithm; non-grain production of winter wheat; winter wheat planting marginalization; Huang–Huai–Hai Plain

## 1. Introduction

Winter wheat, a key grain crop in China and globally [1–3], necessitates comprehensive mapping for winter wheat and analysis of Non-Grain Production (NGP) associated with it. NGP involves cultivating land for non-food purposes, like cash crops or tree planting [4–6].

Specifically, Non-Grain Production of Winter Wheat (NGPOWW) refers to the shift of winter wheat to non-grain uses. The prominence of NGP has grown notably, prompting a series of pertinent reports. Despite government discouragement and policies such as the “Opinions on Preventing Non-Grain Production on Cultivated Land and Stabilizing Grain Production” [6,7], challenges to food security persist due to cultivated land transfer, urbanization, and ecological degradation [8–10]. Significantly, the substantial transfer of cultivated land has led to food marginalization in major grain-producing areas [11]. Monitoring winter wheat planting area is thus vital for monitoring national stability and fostering sustainable development.

The Huang–Huai–Hai (HHH) Plain, renowned as China’s “golden area” for winter wheat production, plays a pivotal role in safeguarding national food security. This plain contributes approximately 60% to the total national winter wheat production and encompasses over 50% of the national winter wheat planting area [12]. Despite recent favorable trends in winter wheat planting in the HHH Plain [13], challenges persist, including cultivated land marginalization, groundwater depletion, and economic development imbalances [14–17]. The most immediate consequence of these pressures is the NGPOWW. NGPOWW in the HHH Plain holds significant implications, demanding careful attention to ensure future food security.

Spatiotemporally mapping winter wheat and monitoring its NGP are imperative for informing and shaping global food security policies, leveraging advanced remote sensing technologies and big data resources [5,18]. Google Earth Engine (GEE) offers easy access to high-performance computing resources for big data processing. It consolidates numerous public geospatial datasets, encompassing free image resources such as Landsat, MODIS, and Sentinel, along with land use/cover and population distribution data [19]. It is extensively employed across various disciplines, including crop yield estimation [20], winter wheat mapping [21], and flood mapping [22], leveraging machine learning algorithms such as random forests, support vector machines, classification and regression trees, and deep neural networks [23,24]. For example, Zhang et al. [25] utilized GEE and random forest machine learning to analyze the temporal and spatial dynamics of winter wheat planting areas in the North China Plain from 1999 to 2019. Cai et al. [26] developed a novel multiple phenological spectral feature on GEE and employed it as input data for a One-Class Support Vector Machine (OCSVM) to map winter wheat. Based on field survey data, Yao et al. [27] integrated Sentinel-1 and Sentinel-2 data, using random forest in traditional machine learning to screen features, which were then input into a deep neural network for efficient and accurate crop mapping. While supervised classification algorithms encounter limitations due to the scarcity of ground truth data, unsupervised methods face challenges in achieving better performance in crop mapping [28]. The efficient and cost-effective application of supervised methods in crop mapping necessitates the collection of training data, emphasizing the importance of extensive field surveys [3].

Large-scale surveying and mapping often demand substantial time and labor resources for collecting ground reference data in the field [29]. This process, especially during the growing season of crops, can be both costly and risky, impacting the acquisition of accurate and reliable training data [30]. Consequently, some crop mapping studies are confined to a single year [31,32] or resort to utilizing data from a different year when reference data for the mapping year are unavailable [33,34]. However, these approaches hinder long-term series crop mapping, and the quality of training data may suffer from inherent classification errors associated with other crop products [35]. Therefore, automated generation of samples for long-term and large-scale mapping, and which are reusable on GEE without extensive field surveys, remains crucial for achieving efficient and cost-effective crop mapping [36]. This study therefore aims to (1) develop an Auto-Generating Winter Wheat Samples algorithm for mapping (AGWWS) on GEE, (2) employ the OCSVM to accurately obtain AGWWS maps in the HHH Plain in 2000, 2005, 2010, 2015, and 2021, and (3) explore NGPOWW and its associated effects on winter wheat planting behavior spatiotemporally over the past two decades.

## 2. Study Area and Data

### 2.1. Study Area

The HHH Plain, located in the eastern coastal region of China ( $31^{\circ}36'N$ – $40^{\circ}29'N$  and  $112^{\circ}13'E$ – $120^{\circ}53'E$ ) (Figure 1), is bordered by the northern Yanshan Mountains, the western Taihang Mountains, the eastern Bohai Sea and Yellow Sea, and the southern Huai River [37]. Its climate falls within the East Asian Temperate Monsoon Climate zone, characterized by an annual mean temperature ranging between  $8^{\circ}C$  and  $15^{\circ}C$ , and precipitation varying from 500 mm to 1000 mm, gradually decreasing from southeast to northwest [38]. Encompassing Beijing, Tianjin, Hebei, Henan, and Shandong [39], it serves as the “gold zone” for China’s winter wheat cultivation. The prevalent cropping system involves the rotation of winter wheat and summer maize, with winter wheat sown in October and harvested in June of the following year. Cash crops such as cotton, fruit trees, Chinese medicinal materials, peanuts, and oilseeds are also cultivated in the Plain [40]. To enhance the algorithm’s efficiency, the study area was subdivided into a  $1^{\circ} \times 1^{\circ}$  grid within the WGS84 coordinate system, resulting in a total of 87 grids [41].

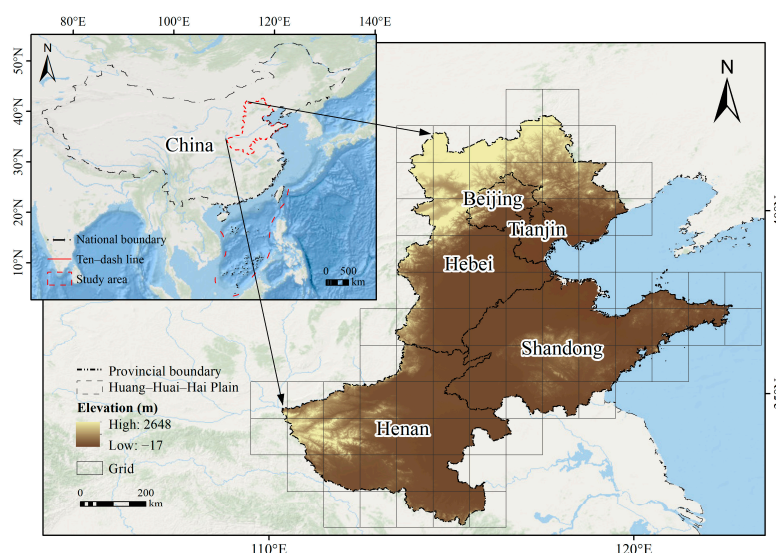


**Figure 1.** The study area and the grids covering the Huang–Huai–Hai Plain.

### 2.2. Datasets

#### 2.2.1. Landsat Surface Reflectance Imagery

This study utilized all available Landsat 5 TM, Landsat 7 ETM+, and Landsat 8 OLI surface reflectance images covering the entire HHH plain on GEE from 1 April to 10 May in 2000, 2005, 2010, 2015, and 2021. In instances where images for a specific year did not meet quality standards or could not cover the study area, adjacent year images (1 April to 10 May of the preceding or subsequent year) were used as replacements. The Landsat TM and ETM+ surface reflectance datasets were derived from the Landsat Ecosystem Disturbance Adaptive Processing System algorithm [42], while the Landsat OLI surface reflectance products were generated employing the Landsat Surface Reflectance Code algorithm [43]. Clouds and cloud shadows were removed from Landsat images utilizing the QA (QA\_PIXEL) band bit mask technique [44]. Specifically, this was achieved by applying bitwise operations to the “QA\_PIXEL” band, which contains encoded data about clouds and shadows. This procedure defines two masks to identify cloud and shadow bits within the QA band, utilizes these masks to create a cloud-free mask, and subsequently applies this mask to the image. This process effectively filters out pixels affected by clouds and shadows, leaving only clear pixels for analysis. Two image collections were formed by merging Landsat 5 and Landsat 7 images into one set and Landsat 7 and Landsat 8 images into another, ensuring the inclusion of all images from each collection. The Landsat 5 and Landsat 7 image collections were used for the years 2000, 2005, and 2010, while the

Landsat 7 and Landsat 8 collections were utilized for 2015 and 2021. By leveraging six spectral bands and calculating three spectral indices for each Landsat image (as detailed in Table 1), composite images were generated by computing median reflectance and index values for each pixel using unmasked pixels.

**Table 1.** Description of spectral bands and vegetation indices.

Band/Index	Wavelength [Min–Max] ( $\mu\text{m}$ )/Equation
Blue (B)	[0.45–0.52]
Green (G)	[0.52–0.60]
Red (R)	[0.63–0.69]
NIR (Near-Infrared)	[0.77–0.90]
SWIR <sub>1</sub> (Shortwave Infrared 1)	[1.55–1.75]
SWIR <sub>2</sub> (Shortwave Infrared 2)	[2.08–2.35]
Normalized Difference Vegetation Index (NDVI) [45]	$\frac{NIR-R}{NIR+R}$
Land Surface Water Index (LSWI) [46,47]	$\frac{NIR-SWIR_1}{NIR+SWIR_1}$
Enhanced Vegetation Index (EVI) [48]	$2.5 * \frac{NIR-R}{(NIR+6*R-7.5*B+1)}$

### 2.2.2. Historical Samples Used to Support the Algorithm for Auto-Generating Samples

The winter wheat maps of the early season in China at 30 m were obtained from Dong et al. [49] (<http://www.nesdc.org.cn/> (accessed on 30 July 2023)). These maps employed a phenology-based method to identify the geographic locations of winter wheat, achieving early winter wheat identification (EWWI) in April with an Overall Accuracy (OA) of 89.88%. The EWWI maps from 2016 to 2021 as historical winter wheat samples were used to support the auto-generating sample algorithm.

## 3. Methods

### 3.1. Auto-Generating Winter Wheat Sample Algorithm

The AGWWS algorithm comprises three main steps, including historical sample generation, optimal threshold determination, and training/validation sample generation (Figure 2). First, historical winter wheat samples were obtained from the EWWI map of 2016 serving as the reference data through a random stratified sampling strategy [50]. The first stratum was the equal-area quadrilateral grids of  $1^\circ \times 1^\circ$  (Figure 1). The second stratum was the two classes in the study area, namely winter wheat and non-winter wheat. Within each grid, the winter wheat and non-winter wheat attributes on the EWWI map were stratified. For the winter wheat attribute, an initial sample size of 1000 was randomly assigned. If the number of winter wheat pixels was less than 1000 within one grid, all winter wheat pixels were selected as the samples for the grid. To address potential classification errors within the EWWI map, unreliable samples were identified and removed based on the observed characteristics of the NDVI and the LSWI of the winter wheat and other crops. The ten-day average time series of winter wheat NDVI and LSWI, along with those of other land use types, including other crops, forest land, built-up land, water, and barren land, were calculated. The observed patterns revealed that during the jointing and heading stages of winter wheat from 1 April to 10 May, winter wheat consistently displayed higher average NDVI and LSWI values compared to other land cover types (Figure 3a). The phenological window from 1 April to 10 May was then employed to distinguish between reliable winter wheat samples and unreliable samples potentially representing other land cover types. Additionally, to obtain reliable crop samples, earlier studies usually retained samples with vegetation indices within their standard deviation range (e.g., Wen et al. [51]). Consequently, we filtered the samples with NDVI and LSWI values outside the standard deviation ranges of NDVI and LSWI (Figure 3b), respectively. Note that this might also have removed some winter wheat samples; however, overall, the samples retained within the standard deviation range were well representative.

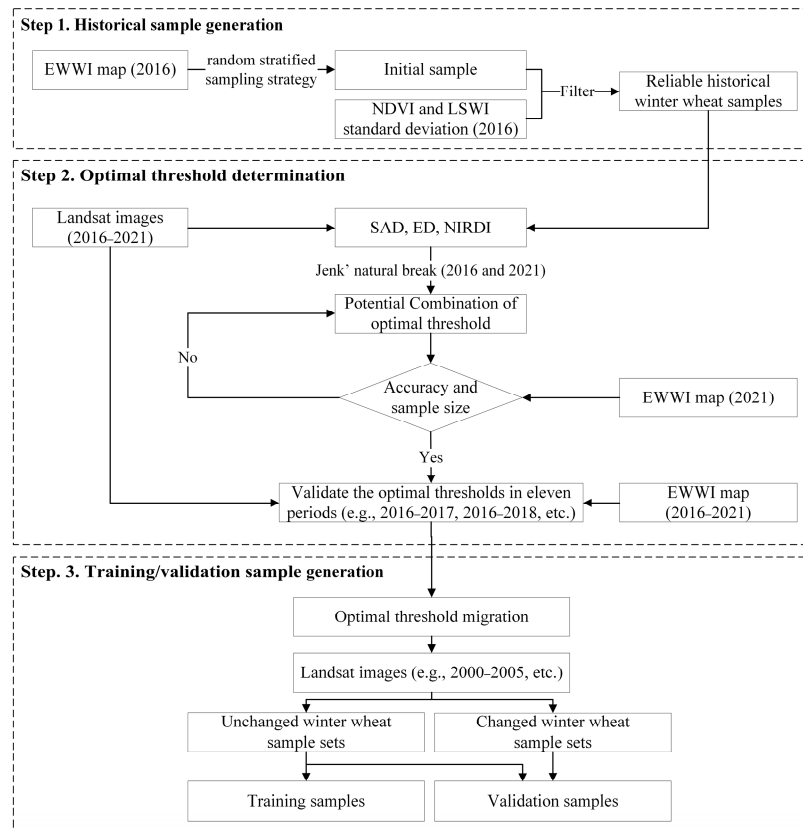


Figure 2. Framework of the Auto-Generating Winter Wheat Samples (AGWWS) algorithm.

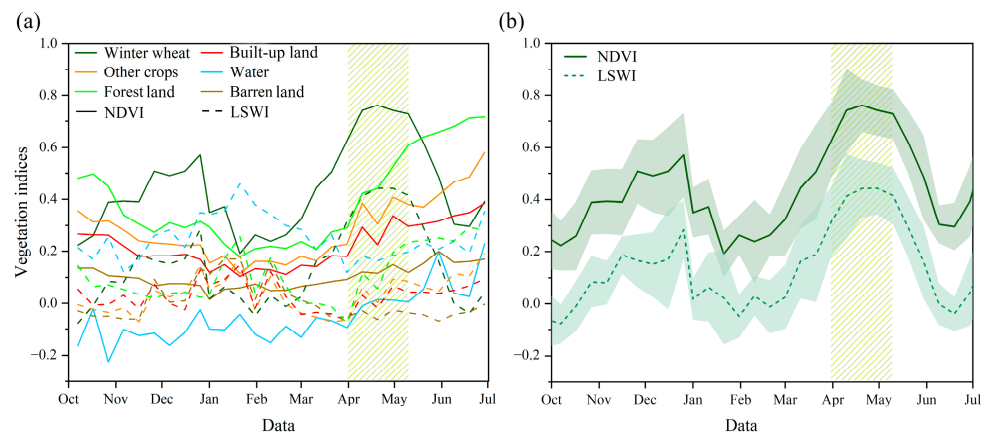


Figure 3. The ten-day average NDVI and LSWI time series for winter wheat and other land cover types (a) and the addition of the standard deviation range on the ten-day average time series of winter wheat, depicted in shaded areas (b). The dotted line represents the phenological window.

Second, using the retained reliable historical samples, the optimal thresholds for detecting winter wheat were determined by measuring the spectral similarity between the reference year (2016) and the target year (2020) on GEE through three indices. These indices are Spectral Angle Distance (SAD, Equation (1)), Euclidean Distance (ED, Equation (2)), and Near-Infrared band Difference Index (NIRDI, Equation (3)). Larger SAD values indicate greater similarity, while smaller ED and NIRDI values signify increased similarity [35]. These indices effectively measure the differences between the reference and target spectra, with SAD and ED offering insights into the magnitude and direction of change between the two [52,53]. NIRDI, reflecting the notably higher average NIR spectral reflectance of winter wheat compared to other crops during the optimal phenological window (Figure 4), was

crucial in indicating spectral similarity. Qiu et al. [1] also supported the efficacy of the NIR band in distinguishing winter wheat from other crops. Jenks' natural break method [54] was then employed in ArcGIS version 10.7 to classify the SAD, ED, and NIRDI of historical winter wheat samples into 5 to 9 categories. This method minimizes the variance within each category of data and maximizes the variance between different categories [55]. It could reasonably test as many potential threshold combinations as possible to determine the optimal combination of the three indices with a sufficient sample size. For each category, distinct thresholds were created by setting intersection criteria based on varying SAD, ED, and NIRDI. The unchanged winter wheat samples were evaluated through OA, Producer's Accuracy (PA), User's Accuracy (UA), and F1 score (Equation (4)) [56], utilizing the EWWI map under each different threshold. The threshold with the highest corresponding OA and that retained a sufficient size of samples was selected as the optimal migration threshold. To validate the performance of the optimal thresholds, they were also applied to eleven periods (from 2016 to 2017, 2016 to 2018, 2016 to 2019, 2016 to 2020, 2016 to 2021, 2017 to 2018, 2017 to 2019, 2017 to 2020, 2018 to 2019, 2018 to 2020, and 2019 to 2020) using the corresponding Landsat images.

$$\theta = \cos^{-1} \frac{\sum_{i=1}^N X_{i(t_1)} Y_{i(t_2)}}{\sqrt{\sum_{i=1}^N (X_{i(t_1)})^2 \sum_{i=1}^N (Y_{i(t_2)})^2}}, SAD = \cos(\theta) \quad (1)$$

$$ED = \sqrt{\sum_{i=1}^N (X_{i(t_1)} - Y_{i(t_2)})^2} \quad (2)$$

$$NIRDI = NIR_{t_1} - NIR_{t_2} \quad (3)$$

$$F1 = \frac{2(PA \times UA)}{(PA + UA)} \quad (4)$$

where  $\theta$  is the spectral angle,  $X_{i(t_1)}$  is the reference spectra when the sample pixel was collected at time  $t_1$ , and  $Y_{i(t_2)}$  is the target spectra to be measured at time  $t_2$ . Variable  $i$  corresponds to the spectral band and ranges from one to the number of bands (N). Here,  $i$  represents bands 1–5 and band 7 for Landsat 5 TM/Landsat 7 ETM+ and bands 2–7 for Landsat 8 OLI. If the reference spectra are identical to the image spectra, SAD is 1, and ED and NIRDI are 0.

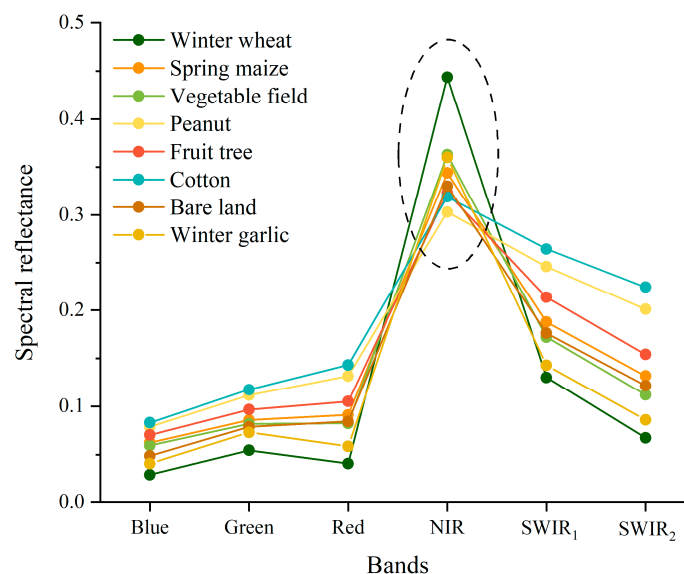


**Figure 4.** Average spectral reflectance of different crop pixels in Landsat images during the optimal phenological window. The dotted circle represents that the average NIR spectral reflectance of winter wheat is higher than that of other crops.

Last, to generate training and validation samples, the optimal threshold was employed to extract unchanged winter wheat sample sets and changed winter wheat sample sets for the periods 2000–2005, 2005–2010, 2010–2015, and 2015–2020. The unchanged sample sets were considered reliable winter wheat samples for the years 2000, 2005, 2010, 2015, and 2020, respectively. These sets served as the input for the classifier to map winter wheat for each respective year. Approximately two-thirds of winter wheat samples and the remaining one-third of winter wheat samples were used, respectively, for training and for validating the mapping method. The non-winter wheat validation samples were generated from the changed winter wheat sample set, maintaining the same ratio as the size of winter wheat validation samples.

### 3.2. One-Class Support Vector Machine for Winter Wheat Mapping

The OCSVM, a supervised one-class classification method within the SVM framework [57], was employed for winter wheat identification due to its superior performance on winter wheat mapping [26]. The OCSVM establishes an optimal hyperplane in the feature space by training on normal data samples. This hyperplane maximizes the interval value, effectively separating the trained samples from their origin [3]. Importantly, it only requires training data from the target class and is used with the Radial Basis Function (RBF) [58]. To conduct the OCSVM, two hyper-parameters, gamma and nu, should be first optimized based on sensitivity analysis [57]. The gamma parameter determines the width of the RBF kernel, whereas nu is the lower limit of the amount of support vectors and the upper limit of the fraction of training samples that are classified as outliers [59]. The analysis was performed based on correlation analysis between classification results under different combinations of the parameters and winter wheat area at the 47-city level from the National Bureau of Statistics (NBS). The combination corresponding to the highest coefficient of determination ( $R^2$ ) was selected as the optimal parameters for the identification. In this paper, the gamma values were tested at 0.05, 0.1, 0.5, 1, 1.5, 2, 2.5, and 5, whilst the nu values were tested at 0.01, 0.05, 0.1, 0.15, 0.2, 0.25, 0.3, 0.35, 0.4, 0.45, and 0.5.

Six spectral bands (bands 1–5 and band 7 for TM 5 and ETM+ 7, and corresponding bands for OLI 8), along with NDVI, LSWI, EVI, elevation, and slope, were used as input features for the OCSVM. The slope data were derived from a 30 m digital elevation model [21]. To identify winter wheat, the optimal phenological window, specifically the jointing and heading stage [21,49], was applied to select time series images. Also, three vegetation indices, NDVI, EVI, and LSWI, were incorporated into the feature set due to their proven efficacy in crop mapping [26,60,61]. Considering the presence of mountains in the study area, two terrain features, elevation and slope, were included in the feature set. The AGWWS maps at 30 m spatial resolution were then generated for 2000, 2005, 2010, 2015, and 2021.

These maps underwent assessment through two primary methods. First, the widely accepted confusion matrix [62] was employed for map accuracy assessment. Note that the AGWWS algorithm could not generate non-winter wheat validation samples for the start year (2000). To overcome this limitation, for the year 2000, validation samples for the non-winter wheat class were randomly selected from the non-cultivated land of China's 30 m annual land cover dataset generated by Yang and Huang in 2021 [63]. A total of 306 non-winter wheat samples were selected and utilized for validation. Second, the winter wheat area derived from the AGWWS map and the EWWI map for 2021 was compared with the winter wheat area reported by the NBS. These two maps were also visually compared. Note that AGSWW maps for 2000, 2005, 2010, and 2015 could not be compared to the unavailable EWWI map.

### 3.3. Spatiotemporally Mapping Non-Grain Production of Winter Wheat

The NGPOWW map depicts the transformation of winter wheat to non-winter wheat focusing on four phases (2000–2005, 2005–2010, 2010–2015, and 2015–2021). To map NGPOWW for each phase, the winter wheat maps of the start and the end years were overlaid

to identify pixels where winter wheat underwent changes. Note that the winter wheat could be transited to another two main crops, maize and paddy rice. Pixels exhibiting this grain-to-grain change were excluded, as this paper solely addresses the grain-to-non-grain issue. To exclude pixels representing the grain-to-grain change, maize maps and paddy rice maps from Luo et al. [64] (<http://dx.doi.org/10.17632/jbs44b2hrk.2> (accessed on 30 July 2023)) for each end year of the first three phases and the maize map from Shen et al. [65] for 2021 (<https://doi.org/10.6084/m9.figshare.17091653> (accessed on 30 July 2023)) were utilized. Maize maps from Luo et al. [64] were resampled to a 30 m resolution. Note that the pixels of winter wheat changed to paddy rice were not removed for 2021 due to the paddy rice map for 2021 currently being unavailable. Nevertheless, the area of winter wheat changed to paddy rice could be disregarded due to its relatively small proportions for each period (Table 2). Additionally, to explore the spatiotemporal pattern of the NGPOWW, the quantile method was employed to evenly categorize the net change in winter wheat area into four levels at the city scale. Cities with NGPOWW areas exceeding  $100 \times 10^3$  ha were chosen for detailed analysis. The NGPOWW characteristics in these representative cities were further analyzed considering the spatial aspects of terrain and land use types.

**Table 2.** The area converted from winter wheat to rice and the proportion of this area converted from winter wheat.

Period	Winter Wheat to Rice ( $\times 10^3$ ha)	Winter Wheat Change ( $\times 10^3$ ha)	Proportion
2000–2005	23.60	3461.30	0.68%
2005–2010	12.60	2483.00	0.51%
2010–2015	52.80	2869.70	1.84%

## 4. Results

### 4.1. Auto-Generating Winter Wheat Samples

A total of 75,846 potential samples were initially obtained from the EWWI map of 2016. Samples outside the standard deviation range of NDVI and LSWI were subsequently filtered, resulting in a total of 16,971 reliable historical winter wheat samples for determining the optimal migration threshold. Table 3 presents the different thresholds created based on intersection criteria within the ninth category, with the remaining categories from 5 to 8 available in the Supplementary Materials. The Group 5 threshold of category 9, corresponding to the highest OA of 95.07% (Figure 5a), were preliminarily identified as the optimal migration thresholds. The size of the associated unchanged winter wheat samples within the historical dataset was 9558. The UA, PA, and F1 scores of the unchanged samples reached 97.90%, 96.41%, and 97.15%, respectively. For changed samples, the UA, PA, and F1 scores were 77.98%, 85.98%, and 81.79%, respectively (Figure 5b–d). Additionally, applying this threshold to the assessment results from eleven periods showed an average OA of 84.07%. For the unchanged winter wheat maps, the average UA, PA, and F1 score were 91.48%, 85.90%, and 88.39%, respectively. The changed winter wheat maps exhibited average UA, PA, and F1 score values of 68.74%, 77.04%, and 71.98%, respectively (Figure 6). Utilizing the optimal migration threshold, two sets of samples were auto-generated: unchanged winter wheat sample sets and changed winter wheat sample sets (Figure 7). Table 4 displays the sample size of the training sample and the validation sample for mapping winter wheat in 2000, 2005, 2010, 2015, and 2020, along with their corresponding accuracy assessment.

**Table 3.** The different thresholds created based on intersection criteria within the 9th category.

Intersection Criteria		$\geq$ SAD	$\leq$ ED	$\leq$ NIRDI
Different thresholds	1	0.678546	0.339203	0.201108
	2	0.805858	0.264924	0.104253
	3	0.853300	0.205496	0.056761
	4	0.892172	0.152997	0.021987
	5	0.926136	0.110889	−0.004949
	6	0.955699	0.080112	−0.029506
	7	0.978941	0.056054	−0.054408
	8	0.993051	0.034353	−0.085166

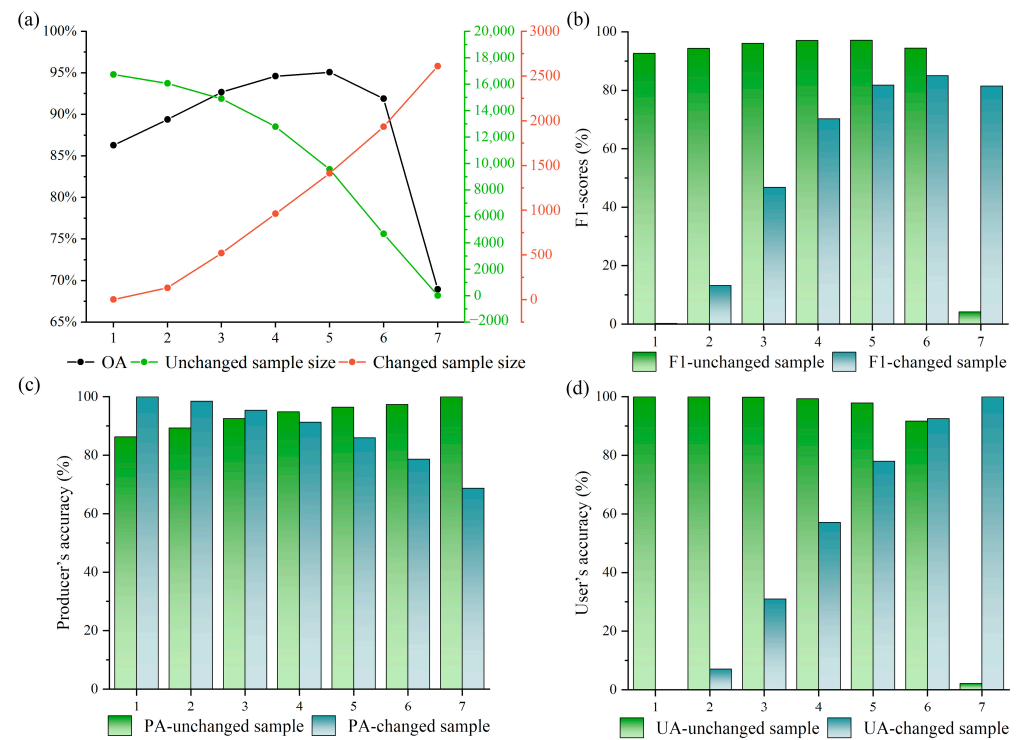


**Figure 5.** Variation of sample size and Overall Accuracy with different thresholds (a), F1 score (b), the Producer's Accuracy (c), and the User's Accuracy (d).

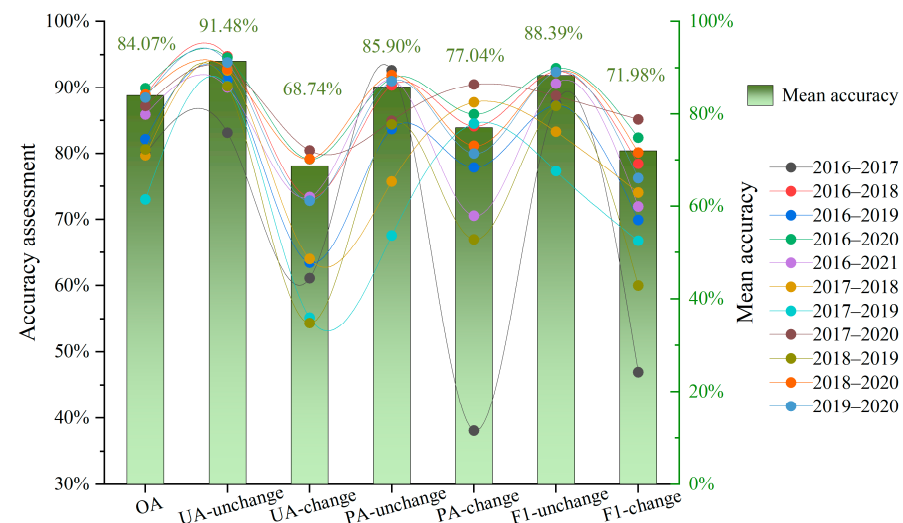


**Figure 6.** Validating the performance of the optimal threshold across eleven periods by utilizing the early winter wheat identification (EWWI) maps.

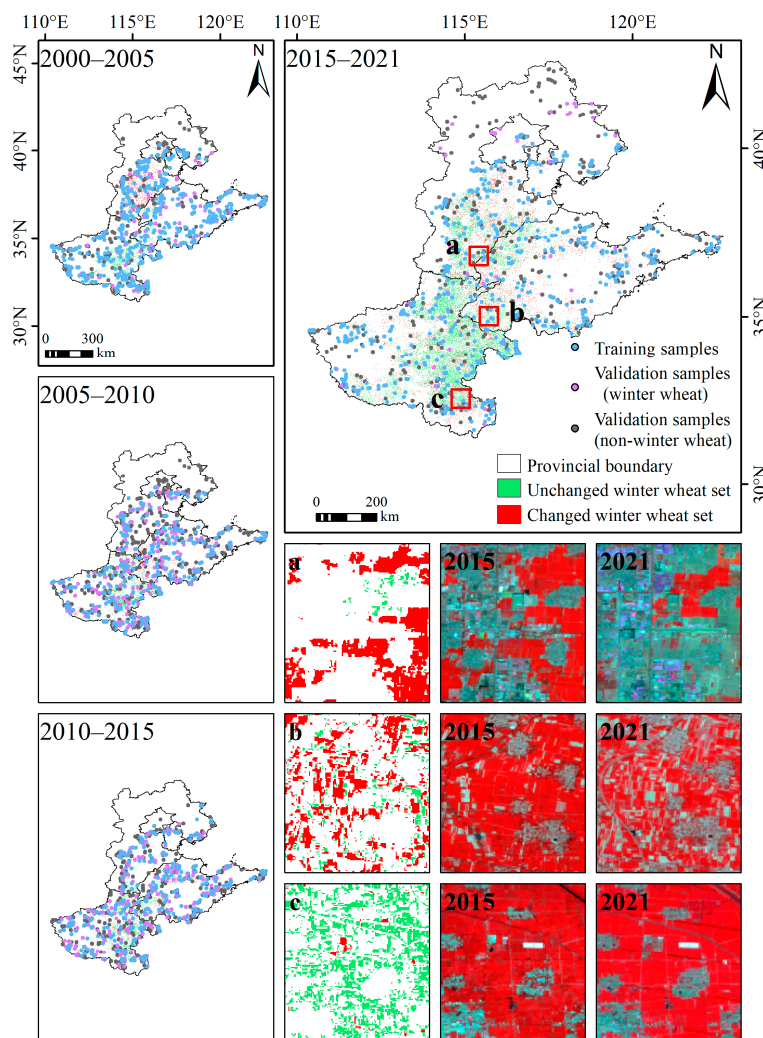


**Figure 7.** The spatial distribution of unchanged and changed winter wheat sample sets in each time period and the distribution of generated training and validation samples on the sample sets. (a–c) represent three spatial details of unchanged and changed winter wheat sample sets from 2015 to 2021, respectively, along with the corresponding Landsat imagery changes.

**Table 4.** The size of training samples and validation samples for each year.

Year	Training Samples		Validation Samples	
	Winter Wheat	Non-Winter Wheat	Winter Wheat	Non-Winter Wheat
2000	642	306	345	306
2005	631	361	316	361
2010	644	361	332	361
2015	644	347	332	347
2021	671	405	353	405

#### 4.2. AGWWS Maps

The significance ranking of  $R^2$  for different parameter combinations shows that the parameter combinations with relatively higher  $R^2$  are concentrated when gamma is 0.05, 0.1, and 0.5 and nu is 0.01, 0.05, 0.1, 0.15, and 0.2 in 2021 (Figure 8). The sensitivity analysis for other years was conducted on these parameter combinations. The highest  $R^2$  values for 2000, 2005, 2010, 2015, and 2021 were 0.77, 0.77, 0.80, 0.86, and 0.87, respectively. The optimal gamma and nu under the highest  $R^2$  values were 0.1 and 0.01, 0.1 and 0.01, 0.1 and 0.1, 0.1 and 0.05, and 0.05 and 0.01, respectively.

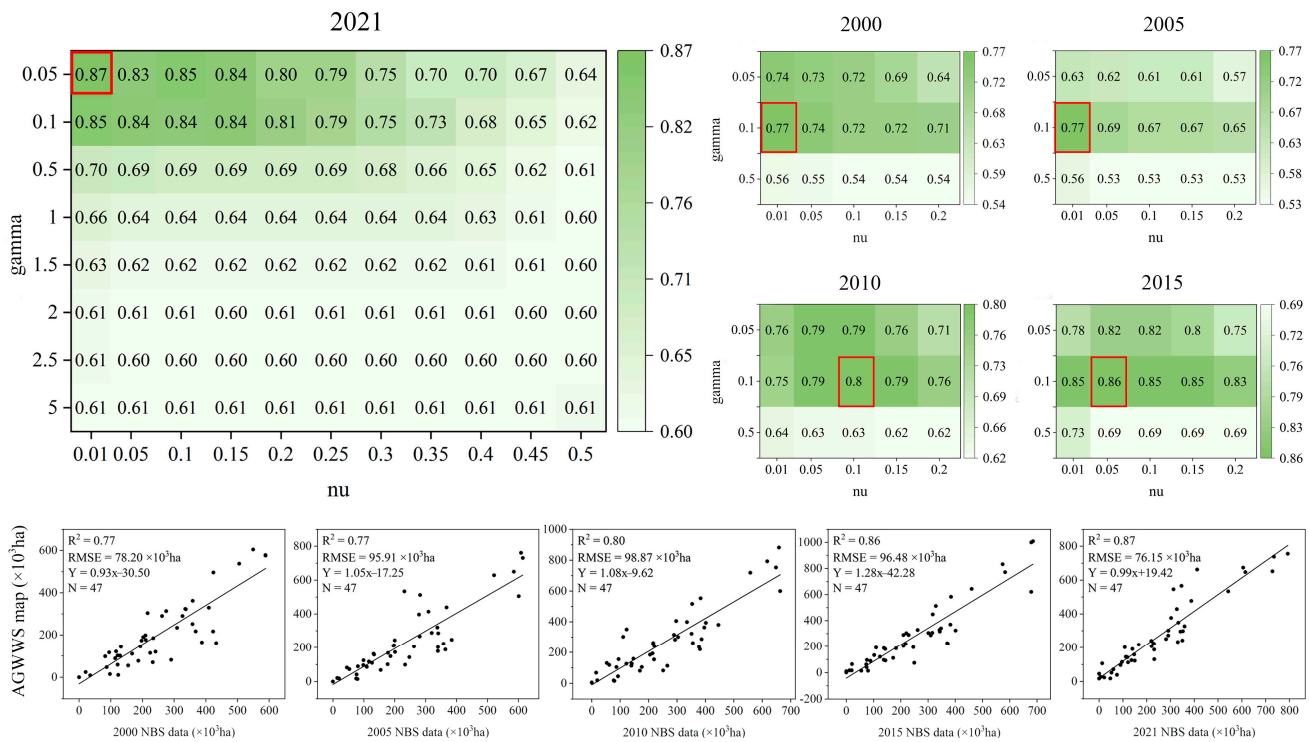


**Figure 8.** The significance ranking of  $R^2$  under different parameter combinations and the correlation analysis between the winter wheat area depicted in AGWWS maps and the winter wheat area at the 47-city level from the National Bureau of Statistics.

The OA of AGWWS maps exceeded 82%, except for 2000 (77.27%) and 2010 (79.37%), with the highest OA observed in 2021 (85.96%) (Table 5). The average OA of all AGWWS maps reached 81.65%. The average UA, PA, and F1 scores for winter wheat were 87.21%, 77.32%, and 80.43%, respectively, while for non-winter wheat, they were 80.27%, 85.05%, and 82.24%, respectively. When compared to the available EWWI map in 2021, the errors of the EWWI map and AGWWS map were 19.90% and 6.55%, respectively. Specifically, the winter wheat planting area reported in the EWWI map for the study area was  $14,457.29 \times 10^3$  ha, the AGWWS map reported  $12,852.83 \times 10^3$  ha, and the NBS indicated an area of  $12,062.90 \times 10^3$  ha. The EWWI map slightly overestimated the winter wheat planting area in the study area. Additionally, the EWWI maps tended to overestimate the area of winter wheat across various types of land plots, including contiguous large plots (Figure 9a), fragmented plots (Figure 9b,c), and regular-shaped plots (Figure 9d,e). In contrast, the AGWWS maps demonstrated a closer alignment with actual land plot types, offering particularly accurate identification of narrow roads between plots.

**Table 5.** The confusion matrix of the AGWWS maps.

Year	Class	Winter Wheat	Non-Winter Wheat	UA (%)	PA (%)	F1 (%)	OA (%)
2000	Winter wheat	297	100	74.81	86.09	80.05	77.27
	Non-winter wheat	48	206	81.10	67.32	73.57	
2005	Winter wheat	220	20	91.67	69.62	79.14	82.87
	Non-winter wheat	96	341	78.03	94.46	85.46	
2010	Winter wheat	261	72	78.38	78.61	78.50	79.37
	Non-winter wheat	71	289	80.28	80.06	80.17	
2015	Winter wheat	252	37	87.20	75.90	81.16	82.77
	Non-winter wheat	80	310	79.49	89.34	84.12	
2021	Winter wheat	262	24	91.61	76.38	83.31	85.96
	Non-winter wheat	81	381	82.47	94.07	87.89	

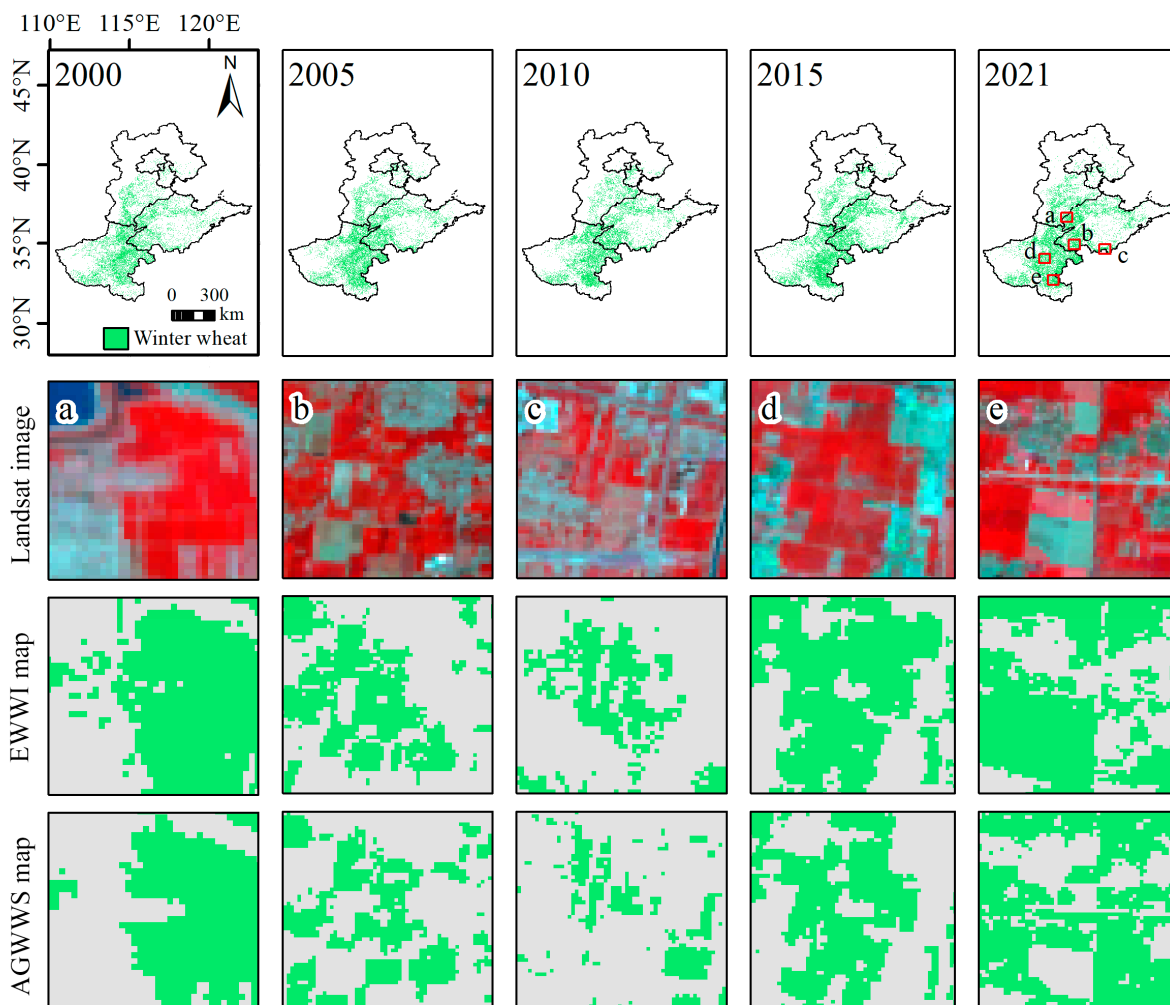


**Figure 9.** AGWWS maps for the study area in 2000, 2005, 2010, 2015, and 2021 (1st row). (a–e) represent the false-color composite of 2021 Landsat images at five different sites (2nd row), with EWWI maps and AGWWS maps at the corresponding sites (3rd and 4th rows).

Winter wheat in the HHH Plain is predominantly concentrated in the flatlands (Figure 9), particularly in the central regions of Hebei Province, the northwest–southwest regions of Shandong Province, and the central and eastern areas of Henan Province. Sparse distribution is observed in northern Hebei, western Henan, and central/eastern Shandong regions, primarily influenced by topographical and economic factors. Northern and western Hebei, characterized by mountainous terrain, prioritize forestry and animal husbandry. In the arid, water-deficient western Henan, extensive dry, thin soil areas make it less suitable for winter wheat cultivation.

The AGWWS maps generally align with the statistical data (Figure 10a). Before 2010, Hebei Province’s (including Beijing and Tianjin) data exhibited significant fluctuations. Post-2010, Shandong Province’s data displayed substantial variability. The change trend in winter wheat area for Henan Province closely resembled the statistical data. While the winter wheat classification results may experience fluctuations due to various factors, they still capture the overall trend in planting area changes. The winter wheat planting area in the study area generally demonstrated an increasing trend from 2000 to 2021, primarily in Shandong and Henan Provinces. In contrast, the winter wheat area in Hebei Province exhibited a “decreasing-increasing” trend before 2010, followed by a decrease after 2010.

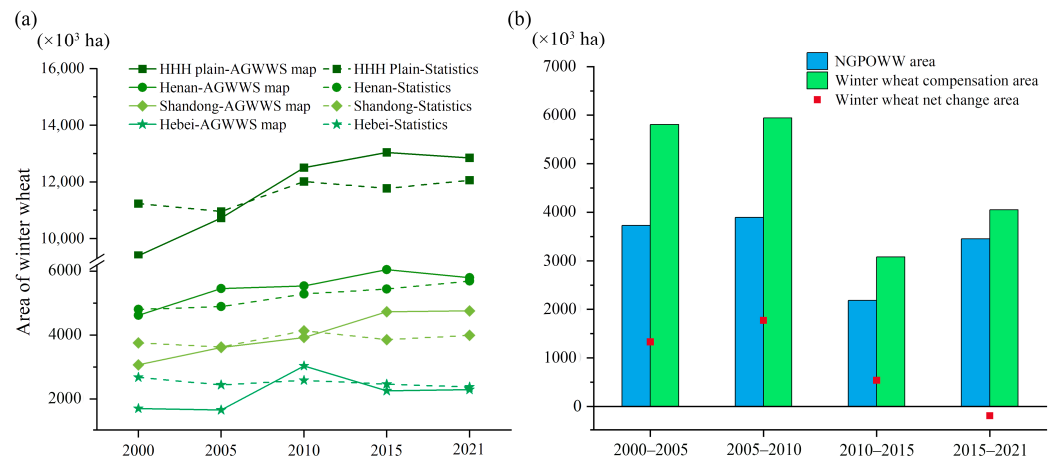


**Figure 10.** Winter wheat area changes over time in AGWWS maps and statistics (a). The Non-Grain Production of Winter Wheat (NGPOWW) area, winter wheat compensation area, and winter wheat net change area during each stage (b).

#### 4.3. Spatiotemporal Pattern of NGPOWW

Figure 10b illustrates the dynamics of NGPOWW in the HHH Plain across four distinct phases. From 2000 to 2005, the NGPOWW area expanded to  $3728.60 \times 10^3$  ha. Subsequently, during the 2005–2010 period, the expansion peaked at  $3894.80 \times 10^3$  ha. A substantial decline occurred from 2010 to 2015, reaching a minimum of  $2182.90 \times 10^3$  ha. The trend shifted from 2015 to 2021, with the NGPOWW area rebounding to  $3451.97 \times 10^3$  ha. Compensation trends for other land use types or crops mirrored the NGPOWW transformation trend. Winter wheat area exhibited continuous growth from 2000 to 2015, followed by a slight decline from 2015 to 2021. This resulted in positive net change areas in the first three stages and a negative net change area of  $-190.88 \times 10^3$  ha from 2015 to 2021.

The results of the quantile method highlight distinct patterns in the net changes of winter wheat area across different regions during specific phases (Figure 11). From 2000 to 2005, regions with lower net changes in winter wheat area were predominantly located in the mountainous or hilly terrains of western and northern Hebei Province, coastal zones in Shandong Province, and hilly areas in the western part of Henan Province. For instance, Binzhou City in the coastal areas of Shandong Province exhibited a higher NGPOWW area but fewer winter wheat compensation areas. Furthermore, in Nanyang City, Henan Province, the NGPOWW area closely matched the winter wheat compensation area. Notably, the winter wheat compensation area primarily expanded in the northwest hilly regions unsuitable for grain cultivation, while the NGPOWW area was concentrated in the central plains.

From 2005 to 2010, cities characterized by high winter wheat planting areas, intricate topography, and rapid urbanization tended to have larger NGPOWW areas. Compared to the first phase, the overall net winter wheat area in Hebei Province showed an increasing trend, while the net change in winter wheat area of some cities in Shandong and Henan Provinces showed a downward trend, including many major grain-producing cities, such as Kaifeng City and Xinyang City in Henan Province. For these two cities, the NGPOWW and winter wheat compensation were mainly distributed in their central and northern areas, but smaller areas of conversion were observed in the southern forestland area.

From 2010 to 2015, the number of cities with NGPOWW areas exceeding  $100 \times 10^3$  ha decreased. Cities exhibiting lower net changes in winter wheat were situated near mountains and hills in Hebei Province, particularly within the rapidly urbanizing Beijing–Tianjin urban agglomeration. Cangzhou City, Hebei Province, stood out as a representative example with cultivated land as the primary land use type. In this region, NGPOWW was concentrated in the northeast and northwest near Beijing and Tianjin, while winter wheat compensation was predominant in the southwest. In contrast to Hebei Province, the plain

regions of Shandong and Henan provinces experienced an increasing trend in winter wheat planting area. For instance, in Zhumadian City, Henan Province, the winter wheat compensation area in the north surpassed the NGPOWW area in the south, resulting in a positive net growth area.

From 2015 to 2021, the number of cities with NGPOWW areas exceeding  $100 \times 10^3$  ha began to rise, particularly in cities characterized by high winter wheat planting areas and rapid urbanization. Notably, the net change in winter wheat area in Hebei Province remained relatively low. Additionally, NGPOWW was concentrated in the eastern plain near the Beijing–Tianjin regions, while winter wheat compensation was distributed in the northeast and southern regions. Furthermore, certain major grain-producing cities in Henan and Shandong Provinces exhibited negative net growth. For instance, Heze City, Shandong Province, displayed a larger NGPOWW area than the winter wheat compensation area, with the latter concentrated in the city’s periphery.

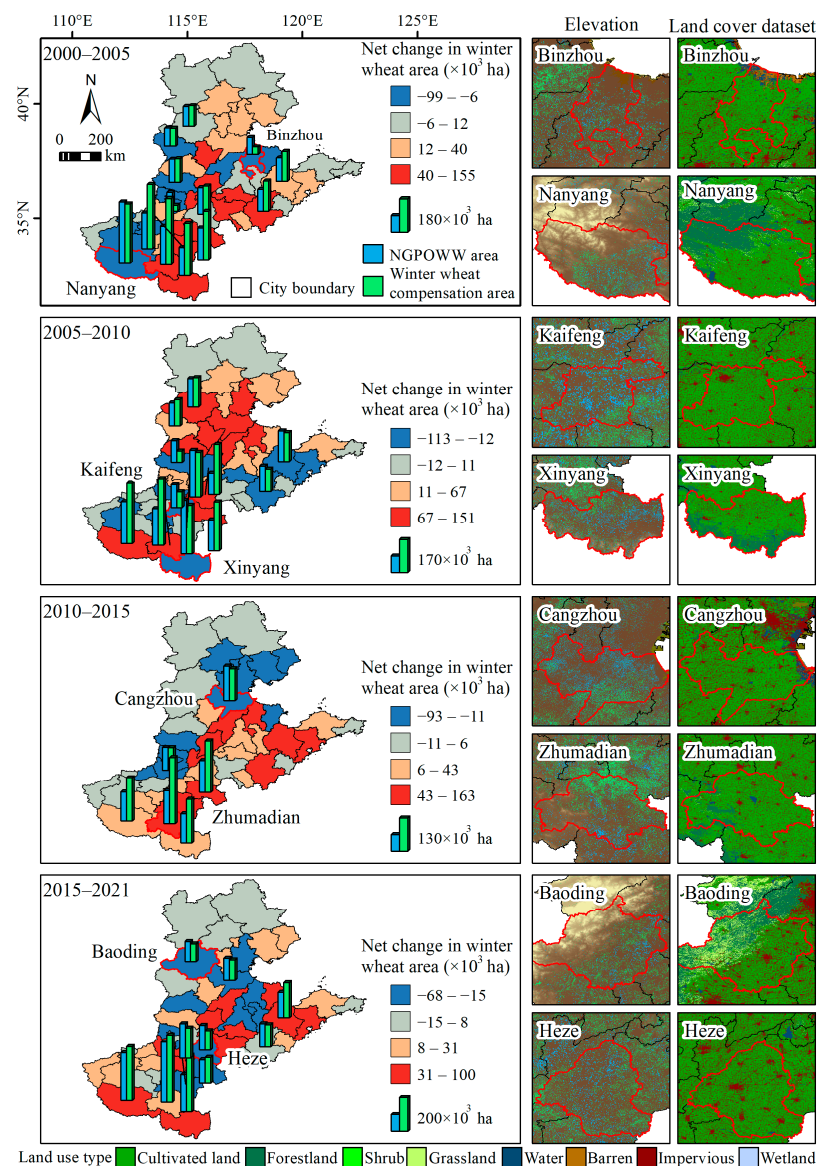


**Figure 11.** Distribution map of winter wheat net change areas by quantile and histograms of NGPOWW area and compensation area (1st column). Distribution of NGPOWW and compensatory planting areas for selected cities (2nd column), along with corresponding land use type distributions (3rd column).

## 5. Discussion

### 5.1. Algorithm Assessment of AGWWS

The determined optimal thresholds of SAD, ED, and NIRDI showed a relatively higher accuracy in extracting unchanged winter wheat samples and changed winter wheat samples across eleven periods. By leveraging the distinctive spectral characteristics of winter wheat within the optimal phenological window, the algorithm effectively differentiates crop samples with similar spectral shapes but varying spectral magnitudes [35]. Using the optimal migration threshold allows for automatically updating the winter wheat sample set in the four periods. This differs from traditional sample migration methods that highly rely on spectral characteristics with ground-labeled samples from historical years [53,66,67]. These characteristics were transferred to the classifiers for the target years lacking samples. The conventional methods demand accurate reference year sample collection, involving significant manpower, time, and financial costs, especially when field-level winter wheat samples are challenging to acquire [66]. In contrast, the AGWWS algorithm does not require continuous field collection efforts or substantial multiple years mapping cost. It automatically and accurately generates training samples by leveraging high spectral similarity between samples solely relying on existing crop maps and remote sensing imagery.

The EWWI maps as key inputs to the AGWWS were thus compared with the AGWWS maps, revealing overestimations of winter wheat area in EWWI maps. A possible reason is the interclass differences in winter wheat, such as varieties of wheat, sowing periods, and irrigation conditions. This poses challenges in distinguishing winter wheat from other crops [49]. In contrast, the integration of the AGWWS algorithm and the OCSVM could accurately identify winter wheat based on reliable auto-generating samples and superior performance in separating target class from the mixed pixels [68].

### 5.2. Spatiotemporally Pattern of Winter Wheat

The spatial results confirm an overall upward trend in winter wheat area in the HHH Plain from 2000 to 2021, aligning with previous findings [13,40,69] and the corresponding statistical data. Three factors contributed to this upward trend. First, the ample sunshine during summer and fall in Henan and Shandong Provinces, coupled with relatively mild winter climates, provides favorable climate conditions for winter wheat cultivation. These climatic advantages have played a pivotal role in promoting the expansion of winter wheat cultivation across the region. Second, the crop's high irrigation requirements find ample support in the abundant water resources of the HHH Plain, strategically situated among the basins of the Yellow River, Hai River, and Yangtze River. This rich water supply has facilitated agricultural development, particularly for crops like winter wheat that thrive with consistent moisture. Last, government policies such as the "National Plan to Increase Grain Production by 100 Billions Kilograms" ([https://www.gov.cn/gzdt/2009-11/03/content\\_1455493.htm](https://www.gov.cn/gzdt/2009-11/03/content_1455493.htm) (accessed on 11 October 2023)) and "China's National Agricultural Water-Saving Outline" ([https://www.gov.cn/zwgk/2012-12/15/content\\_2291002.htm](https://www.gov.cn/zwgk/2012-12/15/content_2291002.htm) (accessed on 11 October 2023)) [70,71] have been instrumental in incentivizing and supporting agricultural practices. These initiatives have played a crucial role in encouraging food production, aligning with broader national goals for food security.

The declining trend in winter wheat cultivation area in Hebei Province since 2010, while noteworthy, has a relatively limited impact on the overall increasing trend observed in the total study area. Urbanization and increased groundwater extraction for irrigation purposes stand out as the primary drivers behind the decline in winter wheat cultivation [72,73]. The escalating costs associated with irrigation have prompted many cities and counties to shift towards cultivating cash crops to enhance economic returns. For instance, Cangzhou City has transitioned to cultivating fruit trees. Handan City is focusing on cotton cultivation. Certain counties in Baoding City are diversifying into industries such as nurseries, fruit trees, and medicinal plants [74]. This shift reflects the complex interplay of economic considerations, resource management, and regional development strategies influencing agricultural land use patterns in Hebei Province.

### 5.3. Marginalization of Winter Wheat Planting Caused by NGPOWW

The marginalization of winter wheat planting occurred in the HHH Plain through four phases, marked by the extensive compensation of winter wheat lands in mountainous regions and city suburbs despite of the overall upward trend in winter wheat area. From 2000 to 2005, Nanyang City exhibited a quantitative balance between the “occupation-compensation” of winter wheat, yet spatially, NGPOWW predominantly spread across the plain regions, with compensatory winter wheat closer to the mountainous northwest area (Figure 11). From 2005 to 2010, sporadic conversions of mountainous forestlands to winter wheat were seen, driven by the loss of winter wheat in the central plains (Figure 11). The winter wheat lands were mainly occupied by special economic crops such as vegetables and fruit trees. For example, from 2000 to 2005 and from 2005 to 2010, Nanyang City and Xinyang City, respectively, showed an increasing trend of the area of special economic crops [75]. This resulted in the “forced uphill” planting of grain.

The current practice of “balance of occupation and compensation” in mountainous regions poses a threat to future food security. First, the rugged terrain of mountains and hills hampers the replacement of labor with agricultural machinery in grain planting, thereby intensifying the challenges faced by farmers [76]. Second, escalating costs associated with grain planting, encompassing labor, fertilizers, and land rent [77] are prompting farmers to increasingly favor cultivating cash crops in mountainous areas. For instance, in Xixia County, Nanyang City, situated in mountainous terrain, the economic returns from crops such as kiwi fruit and mushrooms far exceed those derived from grains in the plains, ensuring substantial agricultural profits [78]. If this trajectory persists, the proliferation of NGPOWW will significantly jeopardize national food security. To prevent further marginalization, future cultivated land regulation should restrict compensation activities in mountainous regions, particularly with the increasing demand for special economic crops. Such strategic interventions are pivotal to maintaining a sustainable balance and safeguarding the long-term viability of winter wheat cultivation in the context of evolving agricultural landscapes.

Additionally, compensation activities occurring in suburban regions due to urbanization negatively affect the sustainability of cultivated land development. Urbanization-driven NGPOWW trends, observed in cities like Binzhou (from 2000 to 2005) and Kaifeng (from 2005 to 2010), are linked to the development of secondary and tertiary industries, placing substantial pressure on grain planting in the southern plains [79,80]. Leveraging a significant consumer market and convenient transportation infrastructure, Kaifeng City emerged as a key national base for planting and exporting cash crops. Its NGPOWW trends were closely tied to its favorable geographic position. The establishment of Xiongan New District near Baoding City in 2017 further exacerbated the situation, inevitably occupying cultivated land and reducing the area available for food planting [81]. From 2010 to 2015, rapid urbanization around Cangzhou City, located in the low plain areas surrounding the Bohai Sea, led to a notable increase in NGPOWW in suburban regions (Figure 11) [82]. This prompted a considerable amount of winter wheat to be planted in the south as compensation, escalating the pressure on grain planting in the southern plains. From 2015 to 2021, Heze City experienced extensive NGPOWW in its central part, with compensation areas closer to the city’s edge (Figure 11) [83]. Heze City, a significant peony export base, has vigorously developed a cultural industry, emerging as a new pillar industry for economic development [84]. These findings confirm that the compensation of winter wheat in the HHH plain frequently occurred due to urbanization. This recurrent pattern of urbanization-induced NGPOWW (the marginalization) poses a significant threat to the sustainability of cultivated land development, aligning with earlier research [11]. Suitable regulations for the “balance of occupation and compensation” of cultivated land are urgently needed to ensure sustainability in the face of evolving urbanization and agricultural landscapes.

#### 5.4. Issues for AGWWS Algorithm and Mapping Winter Wheat

We are aware that the AGWWS algorithm may not perform optimally in the following scenarios due to the biased spectral characteristics of winter wheat in the optimal phenological window. First, areas frequently exposed to extreme weather events, such as droughts or floods, may exhibit spectral characteristics deviating significantly from those of healthy winter wheat [85]. This leads to unreliable samples being used to train the algorithm, consequently reducing its accuracy. Second, new agricultural practices involving new winter wheat varieties can result in spectral characteristics differing significantly from the training samples [86,87]. The optimal migration threshold may not be suitable for identifying these new varieties, posing a challenge for the AGWWS. Last, the rainy or cloudy areas lacking high-quality optical images may not obtain the optimal performance, given the AGWWS's reliance on such images. The low-quality images contaminated by cloud or shadow were replaced by images from the adjacent year in our work. This could potentially lead to biased spectral characteristics being input into the algorithm. The performance of the AGWWS would be negatively impacted. Future work needs to explore how to integrate non-optical imagery such as LiDAR, SAR, or InSAR [88–90] into the AGWWS to improve its accuracy of identification.

The accuracy of winter wheat maps faced two challenges. First, the few Landsat 7 imagery used to fill the data gap when the Landsat 8 OLI and Landsat 5 imagery were unavailable had low quality due to the failure of its scan line corrector. Future work should consider alternative remotely sensed imagery, such as utilizing MODIS data, to mitigate the impact of compromised data quality. Second, given that the OCSVM is sensitive to the spectral noise caused by the landscape heterogeneity [91], cautions must be taken when it is conducted. Future work should entail the training of OCSVM across diverse regions exhibiting distinct landscape heterogeneity. Despite these challenges, the AGSWW maps, characterized by notable accuracy and alignment with NBS data, offer valuable insights into the dynamics of winter wheat cultivation in the HHH Plain from 2000 to 2021.

## 6. Conclusions

This study developed an algorithm for Auto-Generating Winter Wheat Samples (AGWWS). It employs measurements of Spatial Angle Distance (SAD), Euclidean Distance (ED), and Near-Infrared band Difference Index (NIRDI) using historical samples to determine the optimal migration threshold, enabling the auto-generation of winter wheat sample sets for the years 2000, 2005, 2010, 2015, and 2021. The average Overall Accuracy (OA) of winter wheat sample sets is 84.07%. Approximately two-thirds of winter wheat samples and the remaining one-third of winter wheat samples were used, respectively, for training and validating the classifier. The One-Class Support Vector Machine (OCSVM) was employed to map winter wheat for these five years. Based on the correlation analysis between the derived AGWWS maps and the national statistical dataset at the city level, the map with the highest corresponding  $R^2$  was chosen as the AGWWS map for each year (0.77, 0.77, 0.80, 0.86, and 0.87 for 2000, 2005, 2010, 2015, and 2021, respectively). The AGWWS maps ultimately yield an average OA of 81.65%. This study delves into the Non-Grain Production of Winter Wheat (NGPOWW) by analyzing winter wheat change maps from 2000–2005, 2005–2010, 2005–2010, and 2015–2021 in the HHH Plain. Despite an overall increase in the total planted area of winter wheat, the NGPOWW phenomena reveals concerning winter wheat planting marginalization, particularly driven by specialized agriculture and regional economic development. The marginalization was mainly observed in mountainous regions and around suburban regions. This paper emphasizes the need for regulations that restrict occupation and compensation in suitable regions, considering the sustainability of cultivated land development.

**Supplementary Materials:** The following supporting information can be downloaded at: <https://www.mdpi.com/article/10.3390/rs16040659/s1>, Table S1/2/3/4: The different thresholds created based on intersection criteria within the 5/6/7/8th category; Figure S1/2/3/4: Variation of sample size and OA with different thresholds (a), F1 score (b), the PA (c), and the UA (d) within the 5/6/7/8th category.

**Author Contributions:** P.S. initiated the study and was responsible for the examination of the data and revision of the draft; M.Z. conducted the analysis, wrote the first draft, and revised the draft; P.S. and M.Z. jointly completed data curation, the interpretation of data, plotting, and formal analysis; P.S. and Z.S. contributed to supervision, discussion, writing and editing, and the final version. All authors have read and agreed to the published version of the manuscript.

**Funding:** This work was supported by the Natural Science Basic Research Program of the Shaanxi Province of China [grant number 2020]Q-592].

**Data Availability Statement:** Data supporting this study may be provided by the first author upon a reasonable request. The data are not publicly available due to privacy of parts of the data.

**Acknowledgments:** The authors thank the editors and anonymous referees for their valuable comments on an earlier version of this manuscript.

**Conflicts of Interest:** The authors declare no conflicts of interest.

## References

1. Qiu, B.; Luo, Y.; Tang, Z.; Chen, C.; Lu, D.; Huang, H.; Chen, Y.; Chen, N.; Xu, W. Winter Wheat Mapping Combining Variations before and after Estimated Heading Dates. *ISPRS J. Photogramm. Remote Sens.* **2017**, *123*, 35–46. [CrossRef]
2. Upadhyay, P.; Ghosh, S.K.; Kumar, A. Temporal MODIS Data for Identification of Wheat Crop Using Noise Clustering Soft Classification Approach. *Geocarto Int.* **2016**, *31*, 278–295. [CrossRef]
3. Yang, G.; Yu, W.; Yao, X.; Zheng, H.; Cao, Q.; Zhu, Y.; Cao, W.; Cheng, T. AGTOC: A Novel Approach to Winter Wheat Mapping by Automatic Generation of Training Samples and One-Class Classification on Google Earth Engine. *Int. J. Appl. Earth Obs. Geoinf.* **2021**, *102*, 102446. [CrossRef]
4. Zhu, Z.; Dai, Z.; Li, S.; Feng, Y. Spatiotemporal Evolution of Non-Grain Production of Cultivated Land and Its Underlying Factors in China. *Int. J. Environ. Res. Public Health* **2022**, *19*, 8210. [CrossRef]
5. Sun, Y.; Chang, Y.; Liu, J.; Ge, X.; Liu, G.-J.; Chen, F. Spatial Differentiation of Non-Grain Production on Cultivated Land and Its Driving Factors in Coastal China. *Sustainability* **2021**, *13*, 13064. [CrossRef]
6. Zhang, D.; Yang, W.; Kang, D.; Zhang, H. Spatial-Temporal Characteristics and Policy Implication for Non-Grain Production of Cultivated Land in Guanzhong Region. *Land Use Policy* **2023**, *125*, 106466. [CrossRef]
7. State Council General Office. Opinions on Preventing the “Non-Grain” of Production on Cultivated Land and Stabilizing Grain Production. 2020. Available online: [https://www.gov.cn/zhengce/content/2020-11/17/content\\_5562053.htm](https://www.gov.cn/zhengce/content/2020-11/17/content_5562053.htm) (accessed on 11 October 2023).
8. Bindraban, P.S.; van der Velde, M.; Ye, L.; van den Berg, M.; Materechera, S.; Kiba, D.I.; Tamene, L.; Ragnarsdóttir, K.V.; Jongschaap, R.; Hoogmoed, M.; et al. Assessing the Impact of Soil Degradation on Food Production. *Curr. Opin. Environ. Sustain.* **2012**, *4*, 478–488. [CrossRef]
9. Chen, Y.; Li, M.; Zhang, Z. Does the Rural Land Transfer Promote the Non-Grain Production of Cultivated Land in China? *Land* **2023**, *12*, 688. [CrossRef]
10. Satterthwaite, D.; McGranahan, G.; Tacoli, C. Urbanization and Its Implications for Food and Farming. *Philos. Trans. R. Soc. B Biol. Sci.* **2010**, *365*, 2809–2820. [CrossRef]
11. Liu, C.; Song, C.; Ye, S.; Cheng, F.; Zhang, L.; Li, C. Estimate Provincial-Level Effectiveness of the Arable Land Requisition-Compensation Balance Policy in Mainland China in the Last 20 Years. *Land Use Policy* **2023**, *131*, 106733. [CrossRef]
12. National Bureau of Statistics of China. China Statistical Yearbook—2022. National Bureau of Statistics of China. 2022. Available online: <http://www.stats.gov.cn/sj/ndsj/2022/indexch.htm> (accessed on 11 October 2023).
13. Ren, S.; Guo, B.; Wu, X.; Zhang, L.; Ji, M.; Wang, J. Winter Wheat Planted Area Monitoring and Yield Modeling Using MODIS Data in the Huang-Huai-Hai Plain, China. *Comput. Electron. Agric.* **2021**, *182*, 106049. [CrossRef]
14. Su, Y.; Guo, B.; Zhou, Z.; Zhong, Y.; Min, L. Spatio-Temporal Variations in Groundwater Revealed by GRACE and Its Driving Factors in the Huang-Huai-Hai Plain, China. *Sensors* **2020**, *20*, 922. [CrossRef]
15. Tan, Y.; Chen, H.; Xiao, W.; Meng, F.; He, T. Influence of Farmland Marginalization in Mountainous and Hilly Areas on Land Use Changes at the County Level. *Sci. Total Environ.* **2021**, *794*, 149576. [CrossRef]
16. Zhang, Y.; Li, B. Coupling Coordination Analysis of Grain Production and Economic Development in Huang-Huai-Hai Region. *Env. Dev. Sustain.* **2022**, *25*, 13099–13124. [CrossRef]
17. Zhao, X.; Zheng, Y.; Huang, X.; Kwan, M.-P.; Zhao, Y. The Effect of Urbanization and Farmland Transfer on the Spatial Patterns of Non-Grain Farmland in China. *Sustainability* **2017**, *9*, 1438. [CrossRef]

18. Pan, Y.; Li, L.; Zhang, J.; Liang, S.; Zhu, X.; Sulla-Menashe, D. Winter Wheat Area Estimation from MODIS-EVI Time Series Data Using the Crop Proportion Phenology Index. *Remote Sens. Environ.* **2012**, *119*, 232–242. [[CrossRef](#)]
19. Gorelick, N.; Hancher, M.; Dixon, M.; Ilyushchenko, S.; Thau, D.; Moore, R. Google Earth Engine: Planetary-Scale Geospatial Analysis for Everyone. *Remote Sens. Environ.* **2017**, *202*, 18–27. [[CrossRef](#)]
20. Lobell, D.B.; Thau, D.; Seifert, C.; Engle, E.; Little, B. A Scalable Satellite-Based Crop Yield Mapper. *Remote Sens. Environ.* **2015**, *164*, 324–333. [[CrossRef](#)]
21. Fang, P.; Zhang, X.; Wei, P.; Wang, Y.; Zhang, H.; Liu, F.; Zhao, J. The Classification Performance and Mechanism of Machine Learning Algorithms in Winter Wheat Mapping Using Sentinel-2 10 m Resolution Imagery. *Appl. Sci.* **2020**, *10*, 5075. [[CrossRef](#)]
22. Coltin, B.; McMichael, S.; Smith, T.; Fong, T. Automatic Boosted Flood Mapping from Satellite Data. *Int. J. Remote Sens.* **2016**, *37*, 993–1015. [[CrossRef](#)]
23. Chen, C.; McNairn, H. A Neural Network Integrated Approach for Rice Crop Monitoring. *Int. J. Remote Sens.* **2006**, *27*, 1367–1393. [[CrossRef](#)]
24. Jin, Z.; Azzari, G.; You, C.; Di Tommaso, S.; Aston, S.; Burke, M.; Lobell, D.B. Smallholder Maize Area and Yield Mapping at National Scales with Google Earth Engine. *Remote Sens. Environ.* **2019**, *228*, 115–128. [[CrossRef](#)]
25. Zhang, W.; Brandt, M.; Prishchepov, A.V.; Li, Z.; Lyu, C.; Fensholt, R. Mapping the Dynamics of Winter Wheat in the North China Plain from Dense Landsat Time Series (1999 to 2019). *Remote Sens.* **2021**, *13*, 1170. [[CrossRef](#)]
26. Cai, W.; Tian, J.; Li, X.; Zhu, L.; Chen, B. A New Multiple Phenological Spectral Feature for Mapping Winter Wheat. *Remote Sens.* **2022**, *14*, 4529. [[CrossRef](#)]
27. Yao, J.; Wu, J.; Xiao, C.; Zhang, Z.; Li, J. The Classification Method Study of Crops Remote Sensing with Deep Learning, Machine Learning, and Google Earth Engine. *Remote Sens.* **2022**, *14*, 2758. [[CrossRef](#)]
28. SHARMA, R.; GHOSH, A.; JOSHI, P.K. Decision Tree Approach for Classification of Remotely Sensed Satellite Data Using Open Source Support. *J. Earth Syst. Sci.* **2013**, *122*, 1237–1247. [[CrossRef](#)]
29. Zhong, L.; Gong, P.; Biging, G.S. Efficient Corn and Soybean Mapping with Temporal Extendability: A Multi-Year Experiment Using Landsat Imagery. *Remote Sens. Environ.* **2014**, *140*, 1–13. [[CrossRef](#)]
30. Zhang, H.; Du, H.; Zhang, C.; Zhang, L. An Automated Early-Season Method to Map Winter Wheat Using Time-Series Sentinel-2 Data: A Case Study of Shandong, China. *Comput. Electron. Agric.* **2021**, *182*, 105962. [[CrossRef](#)]
31. Peña-Barragán, J.M.; Ngugi, M.K.; Plant, R.E.; Six, J. Object-Based Crop Identification Using Multiple Vegetation Indices, Textural Features and Crop Phenology. *Remote Sens. Environ.* **2011**, *115*, 1301–1316. [[CrossRef](#)]
32. Wardlow, B.D.; Egbert, S.L.; Kastens, J.H. Analysis of Time-Series MODIS 250 m Vegetation Index Data for Crop Classification in the U.S. Central Great Plains. *Remote Sens. Environ.* **2007**, *108*, 290–310. [[CrossRef](#)]
33. Biggs, T.W.; Thenkabail, P.S.; Gumma, M.K.; Scott, C.A.; Parthasaradhi, G.R.; Turrall, H.N. Irrigated Area Mapping in Heterogeneous Landscapes with MODIS Time Series, Ground Truth and Census Data, Krishna Basin, India. *Int. J. Remote Sens.* **2006**, *27*, 4245–4266. [[CrossRef](#)]
34. Turker, M.; Arikan, M. Sequential Masking Classification of Multi-temporal Landsat7 ETM+ Images for Field-based Crop Mapping in Karacabey, Turkey. *Int. J. Remote Sens.* **2005**, *26*, 3813–3830. [[CrossRef](#)]
35. Huang, H.; Wang, J.; Liu, C.; Liang, L.; Li, C.; Gong, P. The Migration of Training Samples towards Dynamic Global Land Cover Mapping. *ISPRS J. Photogramm. Remote Sens.* **2020**, *161*, 27–36. [[CrossRef](#)]
36. Wang, C.; Zhang, H.; Wu, X.; Yang, W.; Shen, Y.; Lu, B.; Wang, J. AUTS: A Novel Approach to Mapping Winter Wheat by Automatically Updating Training Samples Based on NDVI Time Series. *Agriculture* **2022**, *12*, 817. [[CrossRef](#)]
37. Yan, D.H.; Wu, D.; Huang, R.; Wang, L.N.; Yang, G.Y. Drought Evolution Characteristics and Precipitation Intensity Changes during Alternating Dry–Wet Changes in the Huang–Huai–Hai River Basin. *Hydrol. Earth Syst. Sci.* **2013**, *17*, 2859–2871. [[CrossRef](#)]
38. Shirazi, S.Z.; Mei, X.; Liu, B.; Liu, Y. Estimating Potential Yield and Change in Water Budget for Wheat and Maize across Huang-Huai-Hai Plain in the Future. *Agric. Water Manag.* **2022**, *260*, 107282. [[CrossRef](#)]
39. Wang, X.; Zhang, S.; Feng, L.; Zhang, J.; Deng, F. Mapping Maize Cultivated Area Combining MODIS EVI Time Series and the Spatial Variations of Phenology over Huanghuaihai Plain. *Appl. Sci.* **2020**, *10*, 2667. [[CrossRef](#)]
40. Li, J.; Lei, H. Tracking the Spatio-Temporal Change of Planting Area of Winter Wheat-Summer Maize Cropping System in the North China Plain during 2001–2018. *Comput. Electron. Agric.* **2021**, *187*, 106222. [[CrossRef](#)]
41. Yang, G.; Li, X.; Liu, P.; Yao, X.; Zhu, Y.; Cao, W.; Cheng, T. Automated In-Season Mapping of Winter Wheat in China with Training Data Generation and Model Transfer. *ISPRS J. Photogramm. Remote Sens.* **2023**, *202*, 422–438. [[CrossRef](#)]
42. Masek, J.G.; Vermote, E.F.; Saleous, N.E.; Wolfe, R.; Hall, F.G.; Huemmrich, K.F.; Gao, F.; Kutler, J.; Lim, T.-K. A Landsat Surface Reflectance Dataset for North America, 1990–2000. *IEEE Geosci. Remote Sens. Lett.* **2006**, *3*, 68–72. [[CrossRef](#)]
43. Dwyer, J.L.; Roy, D.P.; Sauer, B.; Jenkerson, C.B.; Zhang, H.K.; Lymburner, L. Analysis Ready Data: Enabling Analysis of the Landsat Archive. *Remote Sens.* **2018**, *10*, 1363. [[CrossRef](#)]
44. Zhu, Z.; Wang, S.; Woodcock, C.E. Improvement and Expansion of the Fmask Algorithm: Cloud, Cloud Shadow, and Snow Detection for Landsats 4–7, 8, and Sentinel 2 Images. *Remote Sens. Environ.* **2015**, *159*, 269–277. [[CrossRef](#)]
45. Rouse, J.W.; Haas, R.H.; Schell, J.A.; Deering, D.W. Monitoring Vegetation Systems in the Great Plains with ERTS. *NASA Spec. Publ.* **1974**, *351*, 309.
46. Xiao, X.; Boles, S.; Liu, J.; Zhuang, D.; Liu, M. Characterization of Forest Types in Northeastern China, Using Multi-Temporal SPOT-4 VEGETATION Sensor Data. *Remote Sens. Environ.* **2002**, *82*, 335–348. [[CrossRef](#)]

47. Xiao, X.; Boles, S.; Liu, J.; Zhuang, D.; Frohling, S.; Li, C.; Salas, W.; Moore, B. Mapping Paddy Rice Agriculture in Southern China Using Multi-Temporal MODIS Images. *Remote Sens. Environ.* **2005**, *95*, 480–492. [[CrossRef](#)]
48. Huete, A.R.; Liu, H.; van Leeuwen, W.J. The Use of Vegetation Indices in Forested Regions: Issues of Linearity and Saturation. In Proceedings of the IGARSS'97. 1997 IEEE International Geoscience and Remote Sensing Symposium Proceedings—Remote Sensing—A Scientific Vision for Sustainable Development, Singapore, 3–8 August 1997; IEEE: Piscataway, NJ, USA, 1997; Volume 4, pp. 1966–1968.
49. Dong, J.; Fu, Y.; Wang, J.; Tian, H.; Fu, S.; Niu, Z.; Han, W.; Zheng, Y.; Huang, J.; Yuan, W. Early-Season Mapping of Winter Wheat in China Based on Landsat and Sentinel Images. *Earth Syst. Sci. Data* **2020**, *12*, 3081–3095. [[CrossRef](#)]
50. Xuan, F.; Dong, Y.; Li, J.; Li, X.; Su, W.; Huang, X.; Huang, J.; Xie, Z.; Li, Z.; Liu, H.; et al. Mapping Crop Type in Northeast China during 2013–2021 Using Automatic Sampling and Tile-Based Image Classification. *Int. J. Appl. Earth Obs. Geoinf.* **2023**, *117*, 103178. [[CrossRef](#)]
51. Wen, Y.; Li, X.; Mu, H.; Zhong, L.; Chen, H.; Zeng, Y.; Miao, S.; Su, W.; Gong, P.; Li, B.; et al. Mapping Corn Dynamics Using Limited but Representative Samples with Adaptive Strategies. *ISPRS J. Photogramm. Remote Sens.* **2022**, *190*, 252–266. [[CrossRef](#)]
52. Ji, L.; Geng, X.; Sun, K.; Zhao, Y.; Gong, P. Target Detection Method for Water Mapping Using Landsat 8 OLI/TIRS Imagery. *Water* **2015**, *7*, 794–817. [[CrossRef](#)]
53. Fekri, E.; Latifi, H.; Amani, M.; Zobeidinezhad, A. A Training Sample Migration Method for Wetland Mapping and Monitoring Using Sentinel Data in Google Earth Engine. *Remote Sens.* **2021**, *13*, 4169. [[CrossRef](#)]
54. Jenks, G.F. The Data Model Concept in Statistical Mapping. *Int. Yearb. Cartogr.* **1967**, *7*, 186–190.
55. McMaster, R.B. Automated Line Generalization. *Cartogr. Int. J. Geogr. Inf. Geovisualization* **1987**, *24*, 74–111. [[CrossRef](#)]
56. Zhan, P.; Zhu, W.; Li, N. An Automated Rice Mapping Method Based on Flooding Signals in Synthetic Aperture Radar Time Series. *Remote Sens. Environ.* **2021**, *252*, 112112. [[CrossRef](#)]
57. Ni, R.; Tian, J.; Li, X.; Yin, D.; Li, J.; Gong, H.; Zhang, J.; Zhu, L.; Wu, D. An Enhanced Pixel-Based Phenological Feature for Accurate Paddy Rice Mapping with Sentinel-2 Imagery in Google Earth Engine. *ISPRS J. Photogramm. Remote Sens.* **2021**, *178*, 282–296. [[CrossRef](#)]
58. Xiao, Y.; Wang, H.; Xu, W. Parameter Selection of Gaussian Kernel for One-Class SVM. *IEEE Trans. Cybern.* **2015**, *45*, 941–953. [[CrossRef](#)] [[PubMed](#)]
59. Schölkopf, B.; Platt, J.C.; Shawe-Taylor, J.; Smola, A.J.; Williamson, R.C. Estimating the Support of a High-Dimensional Distribution. *Neural Comput.* **2001**, *13*, 1443–1471. [[CrossRef](#)]
60. Guo, Y.; Xia, H.; Zhao, X.; Qiao, L.; Du, Q.; Qin, Y. Early-Season Mapping of Winter Wheat and Garlic in Huaihe Basin Using Sentinel-1/2 and Landsat-7/8 Imagery. *IEEE J. Sel. Top. Appl. Earth Obs. Remote Sens.* **2022**, *16*, 8809–8817. [[CrossRef](#)]
61. Huang, X.; Huang, J.; Li, X.; Shen, Q.; Chen, Z. Early Mapping of Winter Wheat in Henan Province of China Using Time Series of Sentinel-2 Data. *GIScience Remote Sens.* **2022**, *59*, 1534–1549. [[CrossRef](#)]
62. Congalton, R.G. A Review of Assessing the Accuracy of Classifications of Remotely Sensed Data. *Remote Sens. Environ.* **1991**, *37*, 35–46. [[CrossRef](#)]
63. Yang, J.; Huang, X. The 30 m Annual Land Cover Dataset and Its Dynamics in China from 1990 to 2019. *Earth Syst. Sci. Data* **2021**, *13*, 3907–3925. [[CrossRef](#)]
64. Luo, Y.; Zhang, Z.; Li, Z.; Chen, Y.; Zhang, L.; Cao, J.; Tao, F. Identifying the Spatiotemporal Changes of Annual Harvesting Areas for Three Staple Crops in China by Integrating Multi-Data Sources. *Environ. Res. Lett.* **2020**, *15*, 074003. [[CrossRef](#)]
65. Shen, R.; Dong, J.; Yuan, W.; Han, W.; Ye, T.; Zhao, W. A 30 m Resolution Distribution Map of Maize for China Based on Landsat and Sentinel Images. *J. Remote Sens.* **2022**, *2022*, 9846712. [[CrossRef](#)]
66. Ghorbanian, A.; Kakooei, M.; Amani, M.; Mahdavi, S.; Mohammadzadeh, A.; Hasanlou, M. Improved Land Cover Map of Iran Using Sentinel Imagery within Google Earth Engine and a Novel Automatic Workflow for Land Cover Classification Using Migrated Training Samples. *ISPRS J. Photogramm. Remote Sens.* **2020**, *167*, 276–288. [[CrossRef](#)]
67. Zhang, S.; Yang, J.; Leng, P.; Ma, Y.; Wang, H.; Song, Q. Crop Type Mapping with Temporal Sample Migration. *Int. J. Remote Sens.* **2023**. [[CrossRef](#)]
68. Li, P.; Xu, H.; Guo, J. Urban Building Damage Detection from Very High Resolution Imagery Using OCSVM and Spatial Features. *Int. J. Remote Sens.* **2010**, *31*, 3393–3409. [[CrossRef](#)]
69. Zhou, C.; Zhang, R.; Ning, X.; Zheng, Z. Spatial-Temporal Characteristics in Grain Production and Its Influencing Factors in the Huang-Huai-Hai Plain from 1995 to 2018. *Int. J. Environ. Res. Public Health* **2020**, *17*, 9193. [[CrossRef](#)] [[PubMed](#)]
70. He, C.; Ho, C.-Y.; Yu, L.; Zhu, X. Public Investment and Food Security: Evidence from the Hundred Billion Plan in China. *China Econ. Rev.* **2019**, *54*, 176–190. [[CrossRef](#)]
71. Xu, H.; Yang, R. Does Agricultural Water Conservation Policy Necessarily Reduce Agricultural Water Extraction? Evidence from China. *Agric. Water Manag.* **2022**, *274*, 107987. [[CrossRef](#)]
72. Wang, J.; Liu, H.; Liu, H.; Huang, H. Spatiotemporal Evolution of Multiscale Urbanization Level in the Beijing-Tianjin-Hebei Region Using the Integration of DMSF/OLS and NPP/VIIIRS Night Light Datasets. *Sustainability* **2021**, *13*, 2000. [[CrossRef](#)]
73. Wu, X.; Qi, Y.; Shen, Y.; Yang, W.; Zhang, Y.; Kondoh, A. Change of Winter Wheat Planting Area and Its Impacts on Groundwater Depletion in the North China Plain. *J. Geogr. Sci.* **2019**, *29*, 891–908. [[CrossRef](#)]
74. Pan, X.; Li, G.; Liu, F.; Wu, X.; Kondoh, A.; Shen, Y. Using remote sensing to determine spatio-temporal variations in winter wheat growing area in the North China Plain. *Zgstnyxb* **2015**, *23*, 497–505. [[CrossRef](#)]

75. Henan Provincial Bureau of Statistics. Statistical Yearbook of Henan Province. Henan Provincial Bureau of Statistics. Available online: <https://tj.henan.gov.cn/tjfw/tjcbw/tjnj/> (accessed on 11 October 2023).
76. Li, S.; Li, X. The Mechanism of Farmland Marginalization in Chinese Mountainous Areas: Evidence from Cost and Return Changes. *J. Geogr. Sci.* **2019**, *29*, 531–548. [[CrossRef](#)]
77. Wang, Q.; Qiu, J.; Yu, J. Impact of Farmland Characteristics on Grain Costs and Benefits in the North China Plain. *Land Use Policy* **2019**, *80*, 142–149. [[CrossRef](#)]
78. Chen, C.; Zhao, M. The Undermining of Rural Labor Out-Migration by Household Strategies in China’s Migrant-Sending Areas: The Case of Nanyang, Henan Province. *Cities* **2017**, *60*, 446–453. [[CrossRef](#)]
79. Chen, H.; Xu, L.; Cao, Q.; Huang, M.; Song, M.; Quan, Q.; Liu, J. Coupling and Metabolic Analysis of Urbanization and Environment between Two Resource-Based Cities in North China. *PeerJ* **2019**, *7*, e6869. [[CrossRef](#)]
80. Yang, Y.; Zhang, H.; Qiao, X.; Liu, L.; Zheng, J. Urban Expansion in Major Grain Producing Area from 1978 to 2017: A Case Study of Zhengzhou Metropolitan Area, China. *Chin. Geogr. Sci.* **2023**, *33*, 1–20. [[CrossRef](#)]
81. Luo, J.; Ma, X.; Chu, Q.; Xie, M.; Cao, Y. Characterizing the Up-to-Date Land-Use and Land-Cover Change in Xiong’an New Area from 2017 to 2020 Using the Multi-Temporal Sentinel-2 Images on Google Earth Engine. *ISPRS Int. J. Geo-Inf.* **2021**, *10*, 464. [[CrossRef](#)]
82. Tang, Z.; Zhang, Z.; Zuo, L.; Wang, X.; Zhao, X.; Liu, F.; Hu, S.; Yi, L.; Xu, J. Spatial Evolution of Urban Expansion in the Beijing–Tianjin–Hebei Coordinated Development Region. *Sustainability* **2021**, *13*, 1579. [[CrossRef](#)]
83. Wang, F.; Yuan, X.; Xie, X. Dynamic Change of Land Use/Land Cover Patterns and Driving Factors of Nansihu Lake Basin in Shandong Province, China. *Environ. Earth Sci.* **2021**, *80*, 180. [[CrossRef](#)]
84. Wang, G. Research on Big Data Platform Design in the Context of Digital Agriculture: Case Study of the Peony Industry in Heze City, China. *Contemp. Soc. Sci.* **2022**, *7*, 45–58. [[CrossRef](#)]
85. Wang, S.; Chen, J.; Shen, M.; Shi, T.; Liu, L.; Zhang, L.; Dong, Q.; Wang, C. Characterizing Spatiotemporal Patterns of Winter Wheat Phenology from 1981 to 2016 in North China by Improving Phenology Estimation. *Remote Sens.* **2022**, *14*, 4930. [[CrossRef](#)]
86. Kremneva, O.Y.; Danilov, R.Y.; Sereida, I.I.; Tutubalina, O.V.; Pachkin, A.A.; Zimin, M.V. Spectral Characteristics of Winter Wheat Varieties Depending on the Development Degree of Pyrenophora Tritici-Repentis. *Precis. Agric.* **2023**, *24*, 830–852. [[CrossRef](#)]
87. Wang, C.; Feng, M.; Yang, W.; Ding, G.; Xiao, L.; Li, G.; Liu, T. Extraction of Sensitive Bands for Monitoring the Winter Wheat (*Triticum Aestivum*) Growth Status and Yields Based on the Spectral Reflectance. *PLoS ONE* **2017**, *12*, e0167679. [[CrossRef](#)]
88. Hellwich, O.; Günzl, M.; Wiedemann, C. Fusion of SAR/INSAR Data and Optical Imagery for Landuse Classification. *Frequenz* **2001**, *55*, 129–136. [[CrossRef](#)]
89. Zhou, T.; Pan, J.; Zhang, P.; Wei, S.; Han, T. Mapping Winter Wheat with Multi-Temporal SAR and Optical Images in an Urban Agricultural Region. *Sensors* **2017**, *17*, 1210. [[CrossRef](#)]
90. Höfle, B. Radiometric Correction of Terrestrial LiDAR Point Cloud Data for Individual Maize Plant Detection. *IEEE Geosci. Remote Sens. Lett.* **2014**, *11*, 94–98. [[CrossRef](#)]
91. Yang, X.; Lo, C.P. Using a Time Series of Satellite Imagery to Detect Land Use and Land Cover Changes in the Atlanta, Georgia Metropolitan Area. *Int. J. Remote Sens.* **2002**, *23*, 1775–1798. [[CrossRef](#)]

**Disclaimer/Publisher’s Note:** The statements, opinions and data contained in all publications are solely those of the individual author(s) and contributor(s) and not of MDPI and/or the editor(s). MDPI and/or the editor(s) disclaim responsibility for any injury to people or property resulting from any ideas, methods, instructions or products referred to in the content.